Research Article Vol. 29, No. 19 / 13 Sep 2021 / Optics Express 29755
Optics EXPRESS

Investigation and demonstration of a high-power handling and large-range steering optical phased array chip

LANXUAN ZHANG,[1] YINGZHI LI,[1] YU HOU,[1] YUBING WANG,[2] MIN TAO,[1] BOSONG CHEN,[1] QUANXIN NA,[3] YUXUAN LI,[1] ZIHAO ZHI,[1] XIAOBIN LIU,[1] XUEYAN LI,[1,3] FENGLI GAO,[1] XIANSHU LUO,[4] GUO-QIANG LO,[4] AND JUNFENG SONG[1,3,*]

[1]*State Key Laboratory of Integrated Optoelectronics, College of Electronic Science and Engineering, Jilin University, Changchun, 130012, China*
[2]*State Key Laboratory of Luminescence and Application, Changchun Institute of Optics, Fine Mechanics and Physics, Chinese Academy of Sciences, Changchun, 130010, China*
[3]*Peng Cheng Laboratory, Shenzhen, 518000, China*
[4]*Advance Micro Foundry Pte Ltd, 11 Science Park Road, Singapore Science Park II, Singapore 117685, Singapore*
[*]*songjf@jlu.edu.cn*

Abstract: The optical power handling of an OPA scanning beam determines its targeted detection distance. So far, a limited number of investigations have been conducted on the restriction of the beam power. To the best of our knowledge, we for the first time in this paper explore the ability of the silicon photonics based OPA circuit for the high power application. A 64-channel SiN-Si based one-dimensional (1D) OPA chip has been designed to handle high beam power to achieve large scanning range. The chip was fabricated on the standard silicon photonics platform. The main lobe power of our chip can reach 720 mW and its peak side-lobe level (PSLL) is -10.33 dB. We obtain a wide scanning range of 110° in the horizontal direction at 1550 nm wavelength, with a compressed longitudinal divergence angle of each scanning beam of 0.02°.

1. Introduction

Light Detection and Ranging (LiDAR) is widely applied in ranging, imaging, atmospheric environment detection, three-dimensional vision, autonomous vehicles and more. Integrated optical phased array (OPA) [1–8] is a promising solution of solid-state LiDAR because of its high integration, compact footprint, low cost and compatibility with CMOS technology [9]. It has successfully achieved chip-level target detection [10–12], imaging [13–17] and optical communication [12,18,19].

Most OPAs are silicon-based [2,5,20–23], for which the major concern has been on the scanning features but without much attention to their detection ranging performance. When OPA is applied to target detection, its performance is often affected by the power of the light beam. Higher optical power means higher signal-to-noise ratio, stronger robustness against noise factors, and longer maximum range [24,25]. However, silicon suffers from two photon absorption and free carrier absorption, which makes it unable to handle very high power, as shown by Poulton et al., which measured only 1mW beam power using silicon-based OPA chip [18]. Compared with Si, SiN does not have the nonlinear absorption and it can also be integrated onto SOI platforms. Therefore, it has been considered as a promising alternative to silicon. Some demonstration of SiN OPAs have been shown recently [7,26–29]. However, so far, other than [29] reported the observation of 400 mW main beam power of the SiN OPA, there is no others reported the power performance.

#434067 https://doi.org/10.1364/OE.434067
Journal © 2021 Received 15 Jun 2021; revised 8 Aug 2021; accepted 17 Aug 2021; published 31 Aug 2021

Optics EXPRESS

In this work, a high-power and large-range SiN-Si-based OPA is demonstrated. Silicon nitride is used instead of silicon to transmit light owning to its high-power handling capability. We also conduct a detailed investigation of the laser damage threshold of Si and plasma-enhanced chemical vapor deposition (PECVD) SiN waveguides of our chip. We explore the OPA's ability to withstand high power and the key factor that determines the main lobe power for the first time. The maximum peak power reaches 720 mW, which is, to the best of our knowledge, the maximum power of OPA main lobe ever reported. We show the demonstration of a 64-channel OPA with sub-wavelength spacing. The demonstration shows a wide scanning range of 110° (± 55°) and the peak side-lobe level (PSLL) of -10.33 dB at operation wavelength of 1550 nm. Additionally, by using an off-chip lens, we compress the longitudinal divergence angle of the 1D OPA chip from 32° to 0.02°.

2. Investigation of laser damage of optical waveguides

2.1. Si Waveguide

In order to investigate the laser damage threshold of the Si waveguides, we input pulsed laser light with the 10 ns pulse width and the 100 kHz repetition rate. The coupling loss and transmission loss of silicon waveguide under pulse light are measured by using cutback method. In general, the propagation of photons in waveguides can be simply described by:

$$P_{out} = P_{in}\Gamma \exp(-L\overline{\alpha}) \tag{1}$$

where P_{in} is the input laser power and P_{out} is the output power, $\Gamma = \Gamma_{\text{in}}\ \Gamma_{\text{out}}$, Γ_{in} and Γ_{out} are respectively the input and output coupling efficiency between the lensed fiber and the on-chip spot-size converter (SSC). The SSC used in our experiment is an adiabatic waveguide of 200 μm in length with the width tapering from 0.2 μm to 0.5 μm. L is the length of the waveguide. In this experiment, the waveguide is 500 nm in width and 220 nm in thickness. $\overline{\alpha} = 2k_0\overline{n_i}$ is the average absorption coefficient of the waveguide, k_0 is the wave vector, $\overline{n_i} = \frac{1}{L}\int_0^L n_i(z)dz$ is the imaginary part of the average effective index of the waveguide. Taking logarithm of Eq. (1), we obtained:

$$10\lg\frac{P_{out}}{P_{in}} = 10(\lg\Gamma) - 10\lg(e)L\overline{\alpha} \tag{2}$$

We measure five Si waveguides with lengths of 0.30 cm, 0.38 cm, 0.46 cm, 0.54 cm and 0.62 cm, respectively. The laser wavelength is 1550 nm, and the peak power of the pulsed laser is in the range of 0 ~ 2.2 W. The output pulse peak power of five waveguides is shown in Fig. 1(a). When the peak power is small, the output power is linear with the input. When the pulse peak power increases, the output power first increases, and reaches the maximum at the input peak power of ~390 mW and then drops. In the case of the same input pulse power, the output peak power of the five waveguides shows a strong linear relationship with the waveguide length. Figure 1(b) shows the total insertion loss in the cases indicated by the five black arrows in Fig. 1(a). It is consistent with the linear relationship described in Eq. (2). Figures 1(c) and 1(d) show the coupling loss and propagation loss obtained by linear fitting, respectively. They are strongly dependent on the peak power of the pulse laser. Coupling loss is the corresponding value when L=0 in Eq. (2), the propagation loss is $10\lg(e)\overline{\alpha}$ in Eq. (2). When the pulse peak power is very small, the total coupling loss is ~5dB, which is equivalent to about 2.5 dB/facet, and the propagation loss is about 1.7 dB/cm. The result is close to the 1.9 dB/cm and 1.7 dB/cm measured by a DC low power laser. After that, the coupling loss and propagation loss increase with the increase of pulse peak power, which is due to two-photon absorption and the carrier absorption. Figure 1(d) shows that when the peak power is less than 0.5 W, the transmission loss increases quickly, which is dominated by the two photon absorption in silicon. However, when the power continues to increase, the carriers play a leading role. On the one hand, the carriers have a certain inhibition on the two-photon

Optics EXPRESS

absorption. On the other hand, the carriers have an absorption effect on photons. In this case, as the laser power increases, the propagation loss shows saturation. In the coupling loss in Fig. 1(c), a 200 μm tapered waveguide is considered, so there is also a two-photon absorption component. However, we believe that the mode field distribution of lensed fiber emission becomes wider under high laser power, which leads to serious mode mismatch.

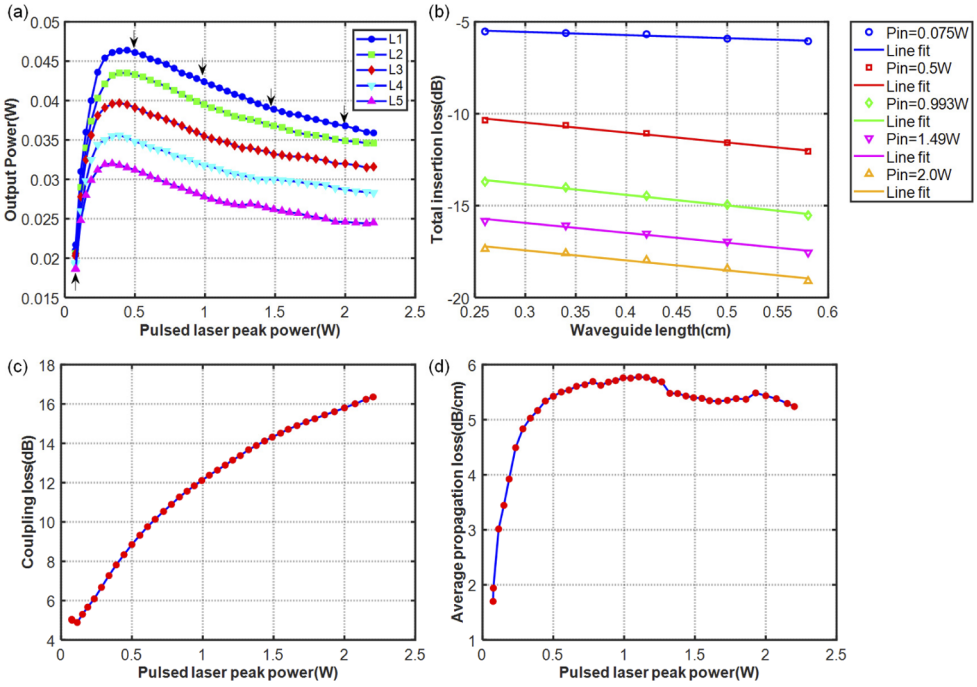

Fig. 1. Before the Si waveguide is damaged by high power, its power transfer situation. (a) The change trend of the output power with input peak power. (b) The relationship between the total insertion loss and the length of the Si waveguide under different input power. (c) Coupling loss between the lensed fiber and waveguide under different pulse peak power. (d) The average propagation loss of Si waveguide under different pulse peak power.

We keep on increasing the peak power, observe the Si waveguide until it is damaged. Record the tipping point at this time, which is the damage threshold of the waveguide. We totally tested 22 Si waveguides, the survival rate of the waveguides under different peak powers (The proportion of waveguides survived under the condition of less than the input peak power, the coupling loss has not been considered) is shown in Fig. 2, the inset illustrates a typical picture of the damaged waveguide. We can conclude that the damage threshold range of Si waveguide is very small, ranging from 2.08 to 2.83 W. According to the fitting curve, when the input peak power Si waveguide is less than 2.15 W, upon which the survival rate of the waveguides can reach 90%. We define this peak power as the damage threshold of the Si waveguide. It can be concluded from Fig. 2 and Fig. 1(a) that the peak power that Si can withstand is relatively small, and the nonlinearity restricts the maximum power which the Si waveguide can transmit, therefore, it also prohibits it from being applicable when dealing with the high optical power.

2.2. PECVD SiN waveguide

Compared with Si, SiN has no nonlinear absorption and can withstand higher power. We use the above-mentioned method to investigate its laser damage threshold. We have tested total 48 PECVD SiN waveguides with the width of 1.5 μm and thickness of 400 nm. The pulse width of

Optics EXPRESS

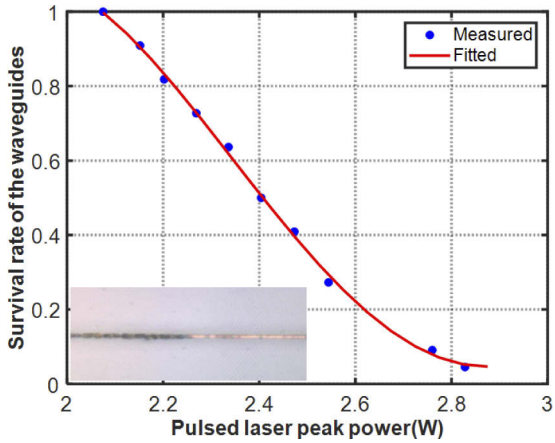

Fig. 2. Survival rate of Si under different input peak power.

the laser is also set at 10 ns with the repetition rate of 100 kHz. The measured result and the fitted are shown in Fig. 3, in which the inset shows the typical damaged waveguide. According to the fitted, we can derive that when the input peak power of SiN is kept less than 35 W, the survival rate of SiN waveguides can be as high as 90%. Therefore, we can define laser damage threshold of SiN waveguide is 35 W. It is worth noting that, the damage power SiN exhibits a wide range from 11.6 to 285 W compared with the previous silicon waveguide. When the peak power in SiN is less than 88 W, 80% of the SiN waveguide is still stable without damage. This demonstrates that most of SiN waveguide can withstand higher power even beyond its defined threshold.

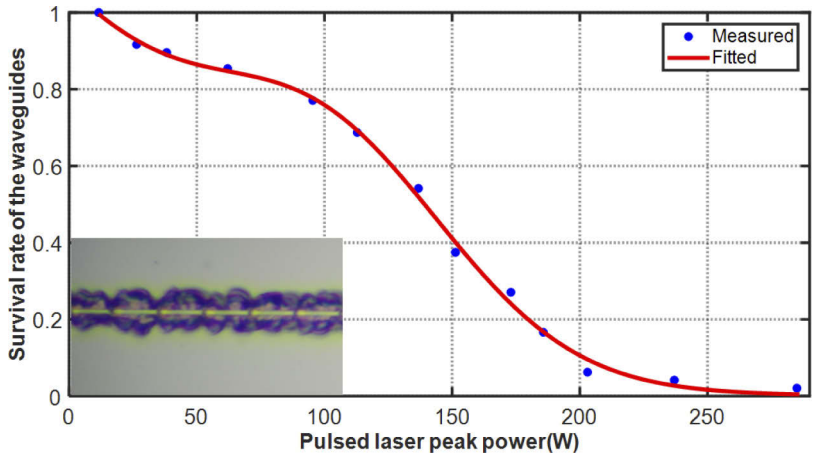

Fig. 3. Survival rate of PECVD SiN under different input peak power.

We have investigated the damage threshold of Si and PECVD SiN waveguides. It can be seen that Si waveguides not only have the lower damage threshold of 2.15 W, but also limit the transmitted power due to the nonlinearity. For SiN waveguides fabricated by PECVD, they have higher damage threshold (as high as 35 W or even higher). Therefore arguably, PECVD SiN waveguides are more suitable for transmitting higher optical power in OPA chips. Considering the steering of OPA, phase-shifting can be implemented in Si using TO effects, whereas in SiN

Optics EXPRESS

the TO efficiency has about one order of magnitude lower power efficiency than in Si [30,31], so we still use Si waveguides in the phase modulation part to achieve optimized beam steering.

3. Fabrication and Experimentation

3.1. Design and fabrication of OPA

The principle of the optical phased array is similar to the multi-slit interference. For the equidistant optical phased array, its scanning range can be obtained by:

$$\theta_{range} = 2\arcsin(0.5\lambda/d) \tag{3}$$

It can be seen that the scanning range is determined by the waveguide spacing. Figure 4 shows the far-field and the extracted intensity distribution of a 64-channel OPA with the waveguide spacing of 5 μm. The grating lobes appear at ±18°, which causes the OPA scanning range to be ±9°, when the OPA steers to 10°, another grating lobe with a little higher intensity appears on the left side and they will become indistinguishable. Obviously, the scanning range of uniform OPA with large spacing is limited by grating lobes. To achieve 180° degree omnidirectional beam steering, the distance between emitters should be half of the wavelength. However, when the distance between waveguides is close, the crosstalk between waveguides must be considered [32]. Simulate the power transmission in equidistant waveguides using FDTD algorithm, as shown in Fig. 5(a), the 12 waveguides have same width of 400 nm and the spacing of 775 nm. Light is incident from the seventh waveguide. The simulation result indicates strong crosstalk between these waveguides, which will eventually lead to non-ideal scanning beam. Many OPAs adopt aperiodic waveguide arrangement with large spacing, which can redistribute the grating lobe power to different positions. Although decreasing the grating lobe power, the signal-to-noise ratio of the scanning beam is sacrificed [23,33,34]. In view of the above disadvantages of large spacing and aperiodic OPA, in this paper, we adopt phase mismatched unequal width waveguide distribution [35]. The waveguide widths are 325 nm, 400 nm, 350 nm, 300 nm and 375 nm respectively, and repeated in this order. We simulated 12 waveguides, light is incident from the 300 nm waveguide, as shown in Fig. 5(b). It can be clearly concluded that when the spacing is also 775 nm, its power can propagate in its own waveguide avoiding crosstalk with other waveguides. This structure not only meets the requirement of large scanning range OPA, but also avoids the crosstalk between waveguides.

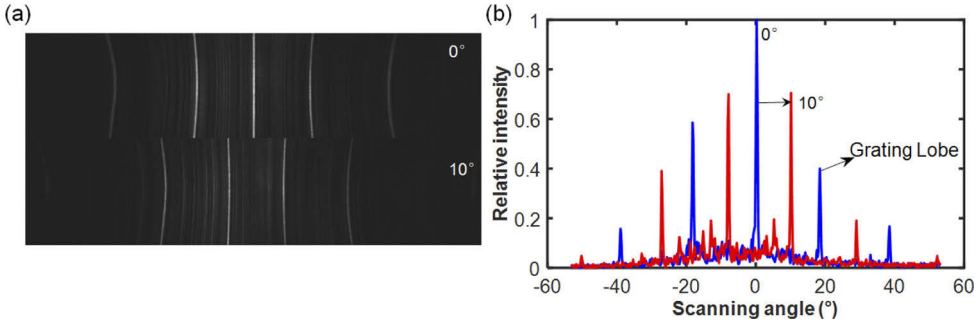

Fig. 4. (a) Far-field of the large spacing OPA. (b) Gray distribution of the steering beams.

Based on the above simulation results, we design and fabricate a 64-channel OPA chip with half wavelength waveguide spacing using standard silicon photonics integration process in AMF, Singapore [36]. The schematic of SiN-Si optical phased array is shown in Fig. 6(a). Due to the high damage threshold of the SiN waveguide, both the incident optical waveguide and Y splitting

Optics EXPRESS

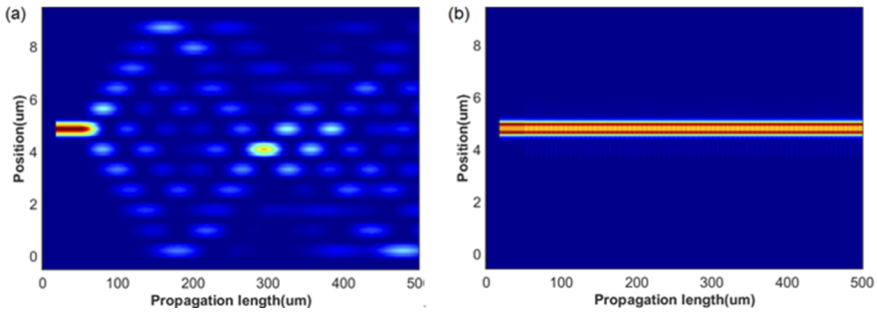

Fig. 5. In the case of sub-wavelength spacing, the power coupling of 12 waveguides. (a) The widths of the waveguide are all 400 nm. (b) The widths of the waveguide are 325 nm, 400 nm, 350 nm, 300 nm and 375 nm respectively.

are performed by SiN waveguides. The Si waveguides are used for thermo-optical modulation and output array. Figure 6(b) shows the optical microscope image of the chip. Figure 6(e) shows the SiN to Si coupling area. The distance between the Si waveguides in this area is 5 μm, the high resistivity heating metal TiN is placed above each Si waveguide to achieve individual control of the phase, as shown in Fig. 6(c). The middle section is the common GND. Figure 6(d) shows the OPA light emitting array. The Si waveguide spacing at the area is reduced to 775 nm, and the waveguide widths are designed according to the above simulation results. In all designs, the width of the waveguide at the final end is reduced to 200 nm.

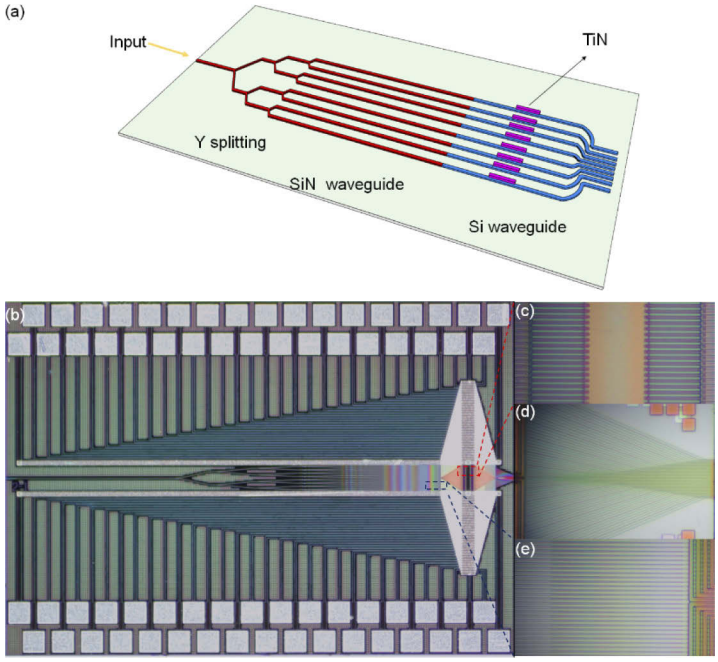

Fig. 6. (a) Schematic diagram of SiN-Si optical phased array chip. (b) Optical microscope picture of SiN-Si optical phased array chip. (c) Phase modulation area. (d) Silicon waveguide light emitting array. (e) SiN-Si coupling area.

Optics EXPRESS

3.2. Experimentation

Figure 7(a) shows the block diagram of the experimental system. Figure 7(b) is the actual characterization setup, using a 1550 nm laser with the electric field transversely polarized as the incident light. The OPA chip is electric-wire bonded to a PCB board which connects to a 64-channel voltage source. The far-field observation screen is positioned 5cm away from the chip. The scale is labelled on the observation screen to calibrate the steering angle, and the infrared camera is used to collect the far-field image and send it to the upper computer. The working process of the upper computer, infrared camera and voltage source is: the upper computer extracts the far-field distribution of the infrared camera under one voltage state, compares it with the ideal distribution pre-defined in the computer, and calculates the similarity between them. After scanning the voltage value for one round, select the voltage value corresponding to the most ideal far-field condition and keep it. Each waveguide repeats the same process until the scanning beam that is closest to the ideal distribution is observed.

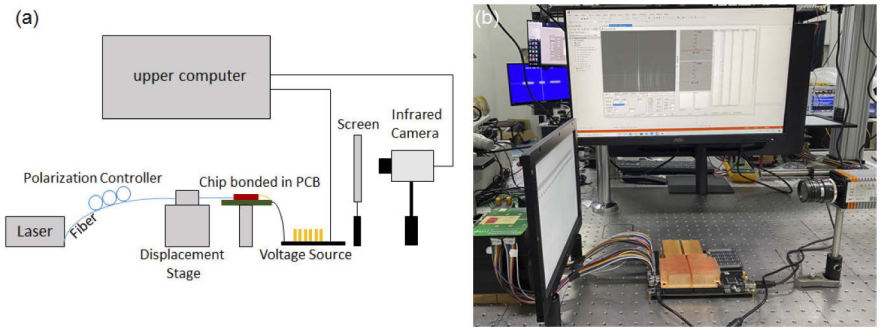

Fig. 7. (a) The block diagram of the experimental system. (b) The actual characterization setup.

In order to obtain the clear far-field beams at all angles, we took the chip as the center and rotated the chip by ±10, 20, 30, 40, 50 and 55 degrees respectively. At this time, the scanning beams corresponding to the above angles point to the center of the screen, which is equivalent to taking the chip as the center and rotating the screen and camera to collect the far-field beam. Figure 8(a) shows the initial far-field and the scanning beams calibrated by the experimental system of the OPA. In the initial state, there are many obvious side lobes and the far-field main lobe is not prominent. This is due to that the phase of the light in the 64 waveguides are not aligned after passing through the respective waveguides. After the phase calibration of upper computer and 64-channel voltage source, clear scanning beams can be obtained. Figure 8(b) shows the extracted intensity distribution of different scanning beams. The intensity is normalized based on the 0° beam. We experimentally achieve a ±55° field of view less than the theoretical ±90°, which is due to the narrow-angle emission from the individual waveguide with the width of 200 nm. As plotted in Fig. 8(c), the peak side lobe level (PSLL) of the 0° scanning beam can reach -10.33 dB. The divergence of 0° and 55° scanning beams are 1.69° and 2.9° separately. They can be compressed by increasing the number of waveguides. When the above 11 angle positions are calibrated, the averaged electric power required for each steering is 1.23W. The main lobe power is measured by focusing the main lobe beam with a Plano-Convex Cylindrical Lens LJ1328L2-C from Thorlabs, when the incident power is 0.89 mW, we can get main lobe with 37 μW optical power, and the total loss is about 13.8 dB of our OPA chip. This total loss includes the fiber-to-chip coupling loss of 1.8 dB, the Y splitter network loss of approximately 2 dB, SiN-Si loss of about 0.2 dB, the loss induced by the lens of about 0.5 dB, and the loss from the side lobe of 9.3 dB.

Optics EXPRESS

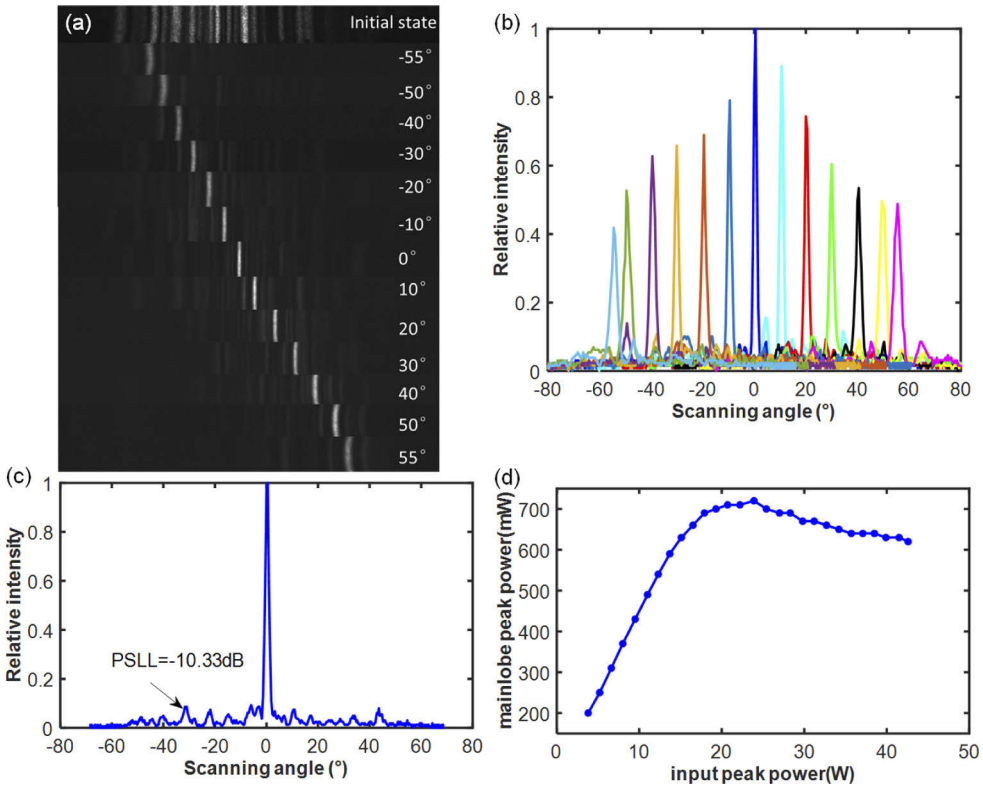

Fig. 8. (a) Far-field of the OPA. (b) Gray distribution of scanning beams. (c) PSLL of 0° beam. (d) The variation trend of main lobe power with the input.

We measure the main lobe power by replacing the light source with a pulsed laser with pulse width of 10 ns, repetition rate of 100 kHz and its peak power increases from 3.8 W to 43 W. As plotted in the Fig. 8(d), when the input peak power of pulse is 24 W, the main lobe peak power reaches the maximum of about 720 mW. This ultra-high power is nearly twice higher in power than the existing demonstration in [29]. The results show that because of the SiN waveguide at the incident end, our SiN-Si-based OPA can withstand high power of 43 W, and the maximum power of the main lobe does not increase linearly with the input power as it is limited by the nonlinearity of the Si waveguide. When the light transmitted to Si waveguide reaches its threshold, it will suffer from the nonlinear effect, while the OPA main lobe power reaches the peak value. If we continue to increase the input power, the main lobe power will decrease.

4. Compression of longitudinal beam

For 1D scanning OPA, the divergence angle of the beam in the horizontal direction is determined by the OPA's aperture size; in the longitudinal direction, it is determined by the thickness of the waveguide. In this end-fire OPA, the waveguide thickness we used is 0.22 μm, and the measured far-field emission angle is 32 degree. In order to compress the longitudinal divergence angle of the far-field beam and increase the laser power to increase the measurement distance, we use the converging characteristics of the convex lens to compress the longitudinal divergence of our OPA chip. We use the Plano-Convex Cylindrical Lens LJ1328L2-C from Thorlabs. When the laser wavelength is 1550 nm, the simulated back focal length is 17.2 mm, by ZEMAX. Figure 9(a) shows the schematic of the experimental system for compressing longitudinal beams. The chip is

Optics EXPRESS

placed above the rotation stage, and the rotation angle of the stage is controlled by the controller. Initially, the chip is at 0 degree, and the Plano-Convex Cylindrical Lens is placed 17 mm in front of the chip, which is fixed by the Kinematic Mount. We put the observation screen at 3 meters away. Figure 9(b) shows the original beam and compressed beam, Fig. 9(c) extracts the longitudinal beam intensity distribution from the position of the red line, it shows that the longitudinal divergence of the 0° beam of the chip is compressed from 32° (the original beam is observed at 10 cm away) to only 0.02°, indicating the longitudinal size of the beam is greatly reduced. In order to measure the compression of the lens for scanning beams at other angles, the chip is rotated by 10°, 20°, 30°, 40°, 50°, 55°, so that the scanning beams at these angles are incident forward to the lens. Figure 9(d) shows the top view of the experimental system and Fig. 9(e) demonstrates the compressed scanning beams of different angles, and their longitudinal intensity distribution is plotted in Fig. 9(f), it shows that the longitudinal divergence of the other beams are also successfully reduced to 0.02°. In a practical application, a laterally curved cylindrical lens can be used, so that all beams are at the focal position, so as to avoid rotating the lens when compressing beams of different angles.

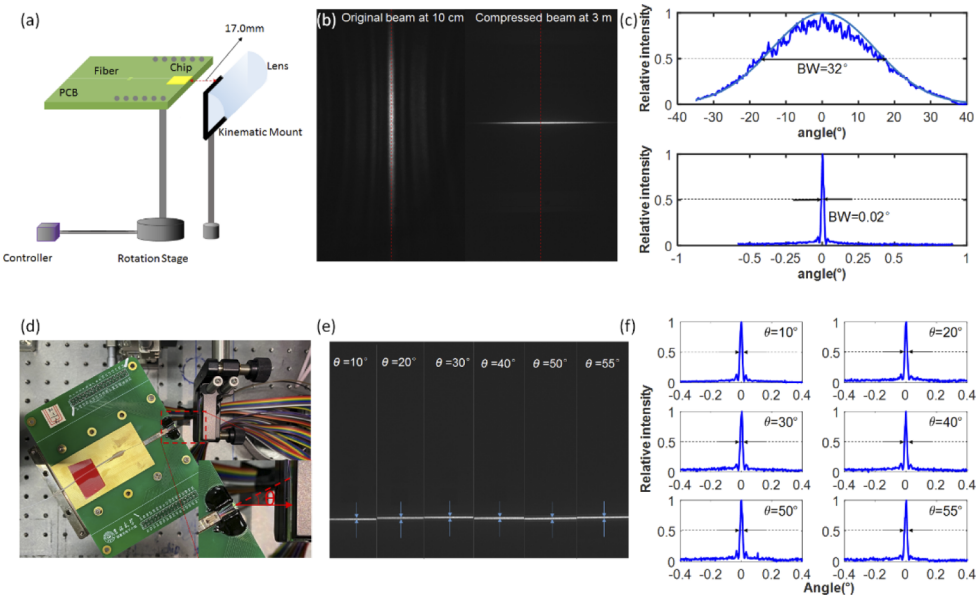

Fig. 9. (a) The characterization setup. (b) The original beam and compressed beam. (c) The longitudinal intensity distribution at the position of the red line of 0° beam. (d) The characterization setup for other scanning beams. (e) The longitudinal compression of other steering beams. (f) The longitudinal beam intensity distribution of other compressed steering beams.

5. Conclusion

In this paper, we investigated the laser power damage threshold of Si and PECVD SiN waveguide. We explored the power of our 64-channel SiN-Si-OPA chip's main lobe, whose peak power can reach as high as 720 mW when the input pulsed laser peak power of 24 W with 10 ns and 100 kHz, which allows for long-range propagation. We conclude that the power of the OPA is limited by the nonlinearity of the Si waveguide at the emitting end, so the main lobe power can be optimized by expanding the number of OPA channels. The phase mismatched waveguide distribution makes the scanning range of the chip up to 110°. For further improvement of the

Optics EXPRESS

scanning range, we can optimize the waveguide width at end for example to 400 nm. At the same time, the longitudinal divergence of the 1D scanning beam is compressed to 0.02° by using the off-chip convex lens, which verifies the feasibility of compressing the longitudinal beam of the 1D OPA, and lays an experimental foundation for the future on-chip integrated lens in 1D chip.

Funding. National Key Research and Development Program of China (2016YFE0200700); National Natural Science Foundation of China (61627820, 61934003, 62090054); Major scientific and technological program of Jilin Province (20200501007GX); Program for Jilin University Science and Technology Innovative Research Team (2021TD-39).

Acknowledgments. We thank Prof. Liu-Qiang Zhang in Chongqing University for spice simulation.

Disclosures. The authors declare that there are no conflicts of interest related to this article.

Data availability. Data underlying the results presented in this paper are not publicly available at this time but may be obtained from the authors upon reasonable request.

References

1. J. Sun, E. Timurdogan, A. Yaacobi, E. S. Hosseini, and M. R. Watts, "Large-scale nanophotonic phased array," Nature **493**(7431), 195–199 (2013).
2. D. N. Hutchison, J. Sun, J. K. Doylend, R. Kumar, J. Heck, W. Kim, C. T. Phare, A. Feshali, and H. Rong, "High-resolution aliasing-free optical beam steering," Optica **3**(8), 887–890 (2016).
3. D. Zhuang, L. Zhagn, X. Han, Y. Li, Y. Li, X. Liu, F. Gao, and J. Song, "Omnidirectional beam steering using aperiodic optical phased array with high error margin," Opt. Express **26**(15), 19154–19170 (2018).
4. W. Xie, T. Komljenovic, J. Huang, M. Tran, M. Davenport, A. Torres, P. Pintus, and J. Bowers, "Heterogeneous silicon photonics sensing for autonomous cars," Opt. Express **27**(3), 3642–3663 (2019).
5. M. Chul Shin, A. Mohanty, K. Watson, G. R. Bhatt, C. T. Phare, S. A. Miller, M. Zadka, B. S. Lee, X. Ji, I. Datta, and M. Lipson, "Chip-scale blue light phased array," Opt. Lett. **45**(7), 1934–1937 (2020).
6. L. Zhang, Y. Li, M. Tao, Y. Wang, Y. Hou, B. Chen, Y. Li, L. Qin, F. Gao, X. Luo, G. Lo, and J. Song, "Large-scale integrated multi-lines optical phased array chip," IEEE Photonics J. **12**(4), 1–8 (2020).
7. C.-S. Im, B. Bhandari, K.-P. Lee, S.-M. Kim, M.-C. Oh, and S.-S. Lee, "Silicon nitride optical phased array based on a grating antenna enabling wavelength-tuned beam steering," Opt. Express **28**(3), 3270–3279 (2020).
8. S. A. Miller, Y.-C. Chang, C. T. Phare, M. C. Shin, M. Zadka, S. P. Roberts, B. Stern, X. Ji, A. Mohanty, O. A. Jimenez Gordillo, U. D. Dave, and M. Lipson, "Large-scale optical phased array using a low-power multi-pass silicon photonic platform," Optica **7**(1), 3–6 (2020).
9. C.-P. Hsu, B. Li, B. Solano Rivas, A. Gohil, P. H. Chan, A. D. Moore, and V. Donzella, "A Review and Perspective on Optical Phased Array for Automotive LiDAR," IEEE J. Sel. Top. Quantum Electron. **27**(1), 1–16 (2021).
10. C. V. Poulton, A. Yaacobi, D. B. Cole, M. J. Byrd, M. Raval, D. Vermeulen, and M. R. Watts, "Coherent solid-state LIDAR with silicon photonic optical phased arrays," Opt. Lett. **42**(20), 4091–4094 (2017).
11. A. Martin, D. Dodane, L. Leviandier, D. Dolfi, A. Naughton, P. O'Brien, T. Spuessens, R. Baets, G. Lepage, P. Verheyen, P. De Heyn, P. Absil, P. Feneyrou, and J. Bourderionnet, "Photonic Integrated Circuit-Based FMCW Coherent LiDAR," J. Lightwave Technol. **36**(19), 4640–4645 (2018).
12. C. V. Poulton, M. J. Byrd, P. Russo, E. Timurdogan, M. Khandaker, D. Vermeulen, and M. R. Watts, "Long-Range LiDAR and Free-Space Data Communication With High-Performance Optical Phased Arrays," IEEE J. Sel. Top. Quantum Electron. **25**(5), 1–8 (2019).
13. F. Aflatouni, B. Abiri, A. Rekhi, and A. Hajimiri, "Nanophotonic coherent imager," Opt. Express **23**(4), 5117–5125 (2015).
14. B. Gao, F. Zhang, E. Zhao, D. Zhang, and S. Pan, "High-resolution phased array radar imaging by photonics-based broadband digital beamforming," Opt. Express **27**(9), 13194–13203 (2019).
15. Y. Kohno, K. Komatsu, R. Tang, Y. Ozeki, Y. Nakano, and T. Tanemura, "Ghost imaging using a large-scale silicon photonic phased array chip," Opt. Express **27**(3), 3817–3823 (2019).
16. H. A. Clevenson, S. J. Spector, L. Benney, M. G. Moebius, J. Brown, A. Hare, A. Huang, J. Mlynarczyk, C. V. Poulton, E. Hosseini, M. R. Watts, R. Dawson, J. P. Laine, and B. F. Lane, "Incoherent light imaging using an optical phased array," Appl. Phys. Lett. **116**(3), 031105 (2020).
17. T. Fukui, Y. Kohno, R. Tang, Y. Nakano, and T. Tanemura, "Single-Pixel Imaging Using Multimode Fiber and Silicon Photonic Phased Array," J. Lightwave Technol. **39**(3), 839–844 (2021).
18. C. V. Poulton, A. Yaacobi, Z. Su, M. J. Byrd, and M. R. Watts, "Optical Phased Array with Small Spot Size, High Steering Range and Grouped Cascaded Phase Shifters," in *Advanced Photonics 2016 (IPR, NOMA, Sensors, Networks, SPPCom, SOF)*, (2016), pp. IW1B.2.
19. S. J. Spector, B. F. Lane, M. R. Watts, L. D. Benney, J. G. Delva, A. E. Hare, A. F. Kelsey, J. M. Mlynarczyk, E. S. Hosseini, C. V. Poulton, and J. P. Laine, "Broadband Imaging and Wireless Communication with an Optical Phased Array," in *Conference on Lasers and Electro-Optics* (Optical Society of America, San Jose, California, 2018), pp. SM3I.7.
20. V. A. Karel, B. Wim, J. Jana, L. T. Nicolas, H. Romuald, and B. Roel, "Off-chip beam steering with a one-dimensional optical phased array on silicon-on-insulator," Opt. Lett. **34**(9), 1477–1479 (2009).

Optics EXPRESS

21. V. A. Karel, R. Hendrik, and B. Roel, "Two-dimensional optical phased array antenna on silicon-on-insulator," Opt. Express **18**(13), 13655–13660 (2010).
22. J. K. Doylend, M. J. R. Heck, J. T. Bovington, J. D. Peters, L. A. Coldren, and J. E. Bowers, "Two-dimensional free-space beam steering with an optical phased array on silicon-on-insulator," Opt. Express **19**(22), 21595–21604 (2011).
23. D. Kwong, A. Hosseini, Y. Zhang, and R. T. Chen, "1×12 Unequally spaced waveguide array for actively tuned optical phased array on a silicon nanomembrane," Appl. Phys. Lett. **99**(5), 051104 (2011).
24. M. Kutila, P. Pyykonen, W. Ritter, O. Sawade, and B. Schaufele, "Automotive LIDAR Sensor Development Scenarios for Harsh Weather Conditions," in *2016 IEEE 19th International Conference on Intelligent Transportation Systems (ITSC)*, (2016), pp. 265–270.
25. M. Kutila, P. Pyykönen, H. Holzhüter, M. Colomb, and P. Duthon, "Automotive LiDAR performance verification in fog and rain," in *2018 21st International Conference on Intelligent Transportation Systems (ITSC)* (2018), pp. 1695–1701.
26. P. Wang, G. Luo, Y. Xu, Y. Li, Y. Su, J. Ma, R. Wang, Z. Yang, X. Zhou, Y. Zhang, and J. Pan, "Design and fabrication of a SiN-Si dual-layer optical phased array chip," Photonics Res. **8**(6), 912–919 (2020).
27. Q. Wang, S. Wang, Y. Zeng, W. Wang, Y. Cai, Z. Tu, W. Yue, X. Wang, Q. Fang, and M. Yu, "Dual-layer waveguide grating antenna with high directionality for optical phased arrays," Appl. Opt. **58**(21), 5807–5811 (2019).
28. N. A. Tyler, D. Fowler, S. Malhouitre, S. Garcia, P. Grosse, W. Rabaud, and B. Szelag, "SiN integrated optical phased arrays for two-dimensional beam steering at a single near-infrared wavelength," Opt. Express **27**(4), 5851–5858 (2019).
29. C. V. Poulton, M. J. Byrd, M. Raval, Z. Su, N. Li, E. Timurdogan, D. Coolbaugh, D. Vermeulen, and M. R. Watts, "Large-scale silicon nitride nanophotonic phased arrays at infrared and visible wavelengths," Opt. Lett. **42**(1), 21–24 (2017).
30. P. Muñoz, G. Micó, L. A. Bru, D. Pastor, D. Pérez, J. D. D. Doménech, J. Fernández, R. Baños, B. Gargallo, R. Alemany, and A. M. Sánchez, "Silicon nitride photonic integration platforms for visible, near-infrared and mid-infrared applications," Sensors **17**(9), 2088 (2017).
31. X. Sun, L. Zhang, Q. Zhang, and W. Zhang, "Si Photonics for Practical LiDAR Solutions," Appl. Sci. **9**(20), 4225 (2019).
32. W. Song, R. Gatdula, S. Abbaslou, M. Lu, A. Stein, W. Y. C. Lai, J. Provine, R. F. W. Pease, D. N. Christodoulides, and W. Jiang, "High-density waveguide superlattices with low crosstalk," Nat. Commun. **6**(1), 7027 (2015).
33. S. Yin, J. H. Kim, F. Wu, P. Ruffin, and C. Luo, "Ultra-fast speed, low grating lobe optical beam steering using unequally spaced phased array technique," Opt. Commun. **270**(1), 41–46 (2007).
34. T. Komljenovic, R. Helkey, L. Coldren, and J. E. Bowers, "Sparse aperiodic arrays for optical beam forming and LIDAR," Opt. Express **25**(3), 2511–2528 (2017).
35. Christopher T. Phare, Min Chul Shin, Jahnavi Sharma, Sohail Ahasan, Harish Krishnaswamy, and A. M. Lipson, "Silicon Optical Phased Array with Grating Lobe-Free Beam Formation Over 180 Degree Field of View," in *Conference on Lasers and Electro-Optics*, (2018), pp. SM3I.2.
36. S. Y. Siew, B. Li, F. Gao, H. Y. Zheng, W. Zhang, P. Guo, S. W. Xie, A. Song, B. Dong, L. W. Luo, C. Li, X. Luo, and G. Q. Lo, "Review of Silicon Photonics Technology and Platform Development," J. Lightwave Technol. **39**(13), 4374–4389 (2021).